Ocean Dynamics (2007) 57: 1–11
DOI 10.1007/s10236-006-0073-2

Christian B. Rodehacke · Hartmut H. Hellmer · Oliver Huhn · Aike Beckmann

Ocean/ice shelf interaction in the southern Weddell Sea: results of a regional numerical helium/neon simulation

Received: 1 June 2005 / Accepted: 11 February 2006 / Published online: 10 May 2006

Abstract Ocean/ice interaction at the base of deep-drafted Antarctic ice shelves modifies the physical properties of inflowing shelf waters to become Ice Shelf Water (ISW). In contrast to the conditions at the atmosphere/ocean interface, the increased hydrostatic pressure at the glacial base causes gases embedded in the ice to dissolve completely after being released by melting. Helium and neon, with an extremely low solubility, are saturation in glacial meltwater by more than 1000%. At the continental slope in front of the large Antarctic caverns, ISW mixes with ambient waters to form different precursors of Antarctic Bottom Water. A regional ocean circulation model, which uses an explicit formulation of the ocean/ice shelf interaction to describe for the first time the input of noble gases to the Southern Ocean, is presented. The results reveal a long-term variability of the basal mass loss solely controlled by the interaction between waters of the continental shelf and the ice shelf cavern. Modeled helium and neon supersaturations from the Filchner–Ronne Ice Shelf front show a "low-pass" filtering of the inflowing signal due to cavern processes. On circumpolar scales, the simulated helium and neon distributions allow us to quantify the ISW contribution to bottom water, which spreads with the coastal current connecting the major formation sites in Ross and Weddell Seas.

Keywords Tracers · Ice shelf water · Antarctic bottom water · Southern ocean · Numerical model

Responsible editor: John Wilkin

C. B. Rodehacke · O. Huhn
University Bremen,
Bremen, Germany

H. H. Hellmer · A. Beckmann
Alfred-Wegener-Institute for Polar and Marine Research,
Bremerhaven, Germany

C. B. Rodehacke (✉)
NASA Goddard Institute for Space Studies,
New York, USA
e-mail: crodehacke@giss.nasa.gov

Present address:
A. Beckmann
University of Helsinki,
Helsinki, Finland

1 Introduction

The sinking of dense water masses at high latitudes drives the ventilation of the global abyss. In the Southern Ocean, the formation of deep and bottom water primarily occurs along the slopes of continental shelves placed in front of the large Antarctic ice shelves, Ross, Amery, and Filchner–Ronne (Baines and Condie 1998) (locations are shown in Fig. 9). Here, heat loss to the atmosphere and related salt gain, due to sea ice formation, reduce the stability of the water column. As a result, deep convection homogenizes the whole water column and transfers salt from the surface to the bottom, thus forming High Salinity Shelf Water (HSSW). This water mass contributes both to the ventilation of the ice shelf caverns and to the formation of new water masses at the continental shelf break. Two mixing processes are known to form deep and bottom water:

– *The Foster–Carmack process* (Foster and Carmack 1976) Pycnocline waters penetrate onto the continental shelf to mix with locally formed HSSW.
– *The Foldvik process* (Foldvik et al. 1985a,b) Ice Shelf Water (ISW), characterized by temperatures below the surface freezing point (Carmack 1974), mixes directly with ambient deep water as it descends the continental slope.

The second process includes the so-called "ice pump" (Lewis and Perkin 1985) circulation, by which near-bottom HSSW flows toward the ice shelf grounding line, driven by gravity and the density contrast between the ice shelf front and the cavern's interior, and controlled by the water column thickness (Gerdes et al. 1999). HSSW is transformed to ISW by cooling below the surface freezing

temperature [due to the pressure dependence of the in situ freezing point (Gade 1979)] and freshening due to deep basal melting (Fig. 1). At the same time, gases captured in the ice matrix during the transformation from snow to ice are released and, due to the high hydrostatic pressure, completely dissolved in the meltwater plume. This results in extreme supersaturations of helium and neon of 1,400 and 1,060%, respectively (Schlosser 1986). Although Hohmann et al. (2002) report helium and neon supersaturations of 1,060 and 770% from the Southeast Pacific, we make use of the former values because our noble gas data in front of the Ronne Ice Shelf support the supersaturation ratio of 0.757 (Fig. 2) reported by Schlosser (1986).

To investigate the importance of ISW for the formation of deep and bottom water, a realistic tracer input was implemented to the regional coupled ice–ocean model BRIOS-1.0 (Beckmann et al. 1999). This paper describes the model setup and the implementation of gas exchange at the atmosphere–ocean and ice shelf–ocean interfaces, as this is a prerequisite for realistic tracer concentrations in an ocean circulation model. For model validation and the identification of the ISW source waters in the Weddell Sea, the paper compares observed and modeled temperature/salinity vs helium distributions. Finally, the spreading path of ISW as part of the new bottom water formed in front of Ross (RIS), Amery, and Filchner–Ronne (FRIS) ice shelves is analyzed.

2 Model description

We use the regional coupled ice–ocean circulation model BRIOS-1.0, which is a modified version of the *s*-coordinate primitive equation model SPEM (Haidvogel et al. 1991, Beckmann et al. 1999). The model comprises the circumpolar Southern Ocean from 50°S to 82°S with a higher isotropic resolution of 1.5° in the Atlantic sector. The major sub-ice shelf caverns are included, but computational restrictions required a water column thickness greater than 200 m. More details of the physical model and its validation are provided in Beckmann et al. (1999),

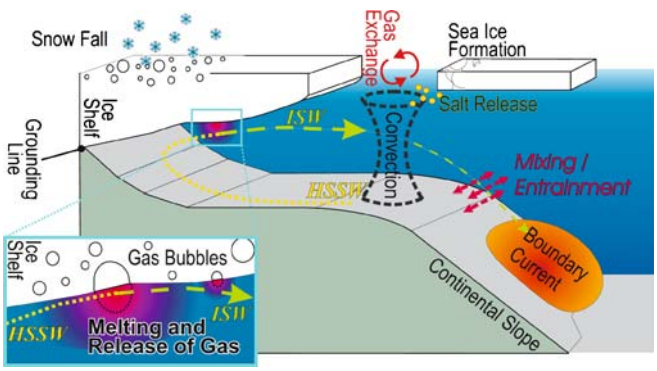

Fig. 1 Schematic of the formation of High Salinity Shelf Water in front and its transformation to Ice Shelf Water within an ice shelf cavern. The *inset* illustrates the transfer of gas from the glacial ice to the meltwater plume

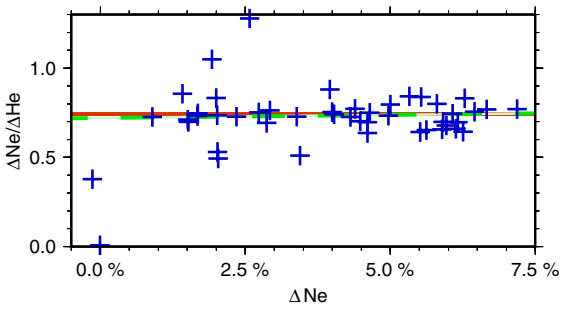

Fig. 2 Ratio of neon/helium supersaturation vs neon supersaturation observed in front of Ronne Ice Shelf during 1995-cruise *ANT XII/3*. Included are the regression line (*green*, *dashed*) and the ratio 1060%/1400%≈0.757 (*red line*) reported by Schlosser (1986)

Timmermann et al. (2002a,b). The ocean model is initialized using temperature and salinity data from the Hydrographic Atlas of the Southern Ocean (Olbers et al. 1992). At the ocean–atmosphere interface, it is driven with a climatological seasonal cycle derived from the stand-alone sea ice/mixed layer model BRIOS-0, which was forced with the European Centre for Medium-Range Weather Forecasts data of the period 1985–1993. The ice shelf–ocean interaction, however, is an integral part of the ocean model; thus, it is computed at every time step.

Due to the lack of reliable gridded data, helium and neon concentrations are initialized with saturation concentrations of 100%. To avoid any supersaturation signal from the northern boundary to influence the results in front of the ice shelves like FRIS, we restored the subsurface saturation at the northern boundary to 97% of the saturation concentration related to the actual temperature and salinity. The time scale of restoring decreased northward from 6 to 1 day over the last six grid boxes. The comparison of integrated supersaturations in front of FRIS, derived from runs with restoration at the northern boundary to reduced saturation and equilibrium saturation, shows that the northern influence is negligible.

The model was integrated for 20 years to reach a quasi-stationary dynamical state (Beckmann et al. 1999). Additional 80 years of integration were performed with noble gas input at the ocean surface. The results were analyzed starting with year 30 since tracer release (year 50 of total model integration) to guarantee quasi-steady state tracer distributions in the area of our scientific interest.

2.1 Tracer boundary condition

The exchange of gaseous tracer at the atmosphere–ocean interface is implemented as a flux boundary condition according to Wanninkhof (1992) and Asher and Wanninkhof (1998). The flux of low-solubility, nonreactive gases depends on the concentration gradient and the wind velocity at the interface. Since the sea ice cover, an important element of the polar climate system, reduces the gas exchange and supports the concentration difference, it is described according to England et al. (1994).

The gas exchange is completely described by:

$$F_G = k_0(\alpha_s p_{\text{atmos}} - c_w)(1 - A)\frac{u^2_{10\text{ m}}}{\sqrt{Sc}}, \quad (1)$$

where k_0 is the piston velocity[1], $\alpha_s \cdot p_{\text{atmos}}$ is the solubility concentration after Weiss (1971), with p_{atmos} representing the atmospheric partial pressure[2] of helium/neon supposed to be constant in space and time, c_w is the concentration at the ocean surface, and (Sc) is the Schmidt number described by Jähne et al. (1987). The sea ice cover A was derived from the sea ice/mixed layer model BRIOS-0; its results agree well with satellite and Upper Looking Sonar data (R. Timmermann, personal communication).

For convenience, the tracer distributions are presented as deviation from their saturation concentration, defined by:

$$\Delta X \overset{\text{def}}{=} \left(\frac{X_{\text{obs}} - X_0}{X_0}\right) \cdot 100, \quad (2)$$

with $X_{\text{obs}} = (\text{Ne}, {}^4\text{He})$ and X_0 as the equilibrium values according to Weiss (1971).

This supersaturation, which depends on the temperature (Θ) and salinity (S), is an appropriate description because a pronounced supersaturation in the water column clearly identifies the ISW contribution. Such distinction cannot be done solely based on the concentration. However, some doubts exist about the accuracy of the solubility curves presented by Weiss (1971). Hamme and Emerson (2004) showed that these curves underestimate neon in cold seawater by 2% and Top et al. (1987) claim that the helium curves are probably too low. Because we initialize the model with equilibrium saturation, the surface flux[3] is driven according to deviations from the saturation concentration, and the results are presented as relations to the saturation concentration; a slightly questionable solubility curve does not significantly affect our results.

2.2 Input by ice shelf basal melting

The input of helium and neon is assumed to be proportional to the ice shelf melt rate, which is calculated at every time step as part of the coupled ice shelf–ocean model according to Hellmer and Olbers (1989). For melting zones, the concentration in the uppermost ocean layer $c_{k=N}$ of the cavern is calculated by:

$$c_{k=N} = -c_0 \hat{S}\left(\frac{\frac{\partial h_{\text{ice}}}{\partial t}\,dt}{\Delta z_{k=N}}\right)_{\frac{\partial h_{\text{ice}}}{\partial t} < 0}, \quad (3)$$

where c_0 is the saturation concentration, $\hat{S}$ is the supersaturation, $\Delta z_{k=N}$ is the height of the upper most ocean grid box, $\partial h_{\text{ice}}/\partial t$ is the melt rate, and dt is the model's time step. This formulation also describes melting at the ice front, as the vertical wall is approximated by an inclined interface due to the use of vertical s-coordinates. The influence of the formation of ice crystals within the cavern and their successive accumulation at the ice shelf based on the noble gas concentration was considered insignificant and thus neglected.

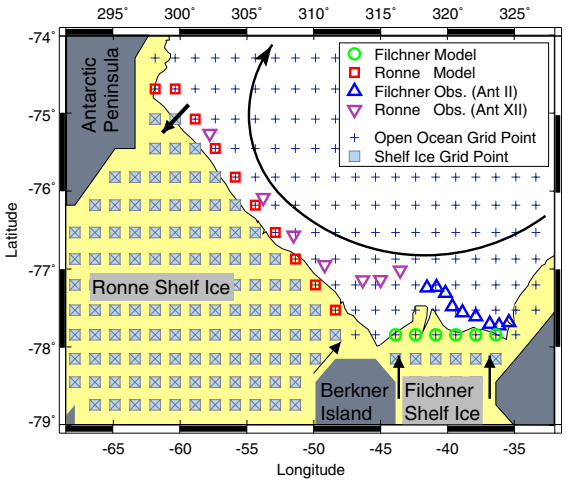

Fig. 3 Locations of hydrographic stations and model grid points related to the model (*dark gray*) and observed (*yellow*) landmask in the southwestern Weddell Sea. Note that the positions of ice shelf edge differ due to ice advance and retreat. *Arrows* schematically represent the main shelf circulation. For details, see text

3 Model validation

The noble gases were sampled close to the Filchner–Ronne Ice Shelf edge at that time (Fig. 3, observed shelf ice edge were taken from a GMT data set[4]). Due to advance and retreat inherent in the ice shelf movement, its position slightly differs from the edge position used in the model (Fig. 3) but has no influence on our comparison of the properties at the ice edge. The distribution of noble gases in front of the Filchner Ice Shelf is presented in detail by Schlosser et al. (1990), while a description for the area off Ronne Ice Shelf is in preparation (O. Huhn, personal communication). The hydrographic conditions on the

[1] Derived from bomb-produced radiocarbon invasion rates into the ocean and, hence, k_0 includes implicitly the Schmidt number for ^{14}C.

[2] We assumed a constant total atmospheric pressure of 992.94 hPa ≈ 0.97996 atm.

[3] The uncertainty in the parameterization of the flux dependence to wind speed has probably a larger effect.

[4] GMT (General Mapping Tool) topography is mainly based on the World Vector Shore data set of the National Geophysical Data Center in Boulder, CO, USA.

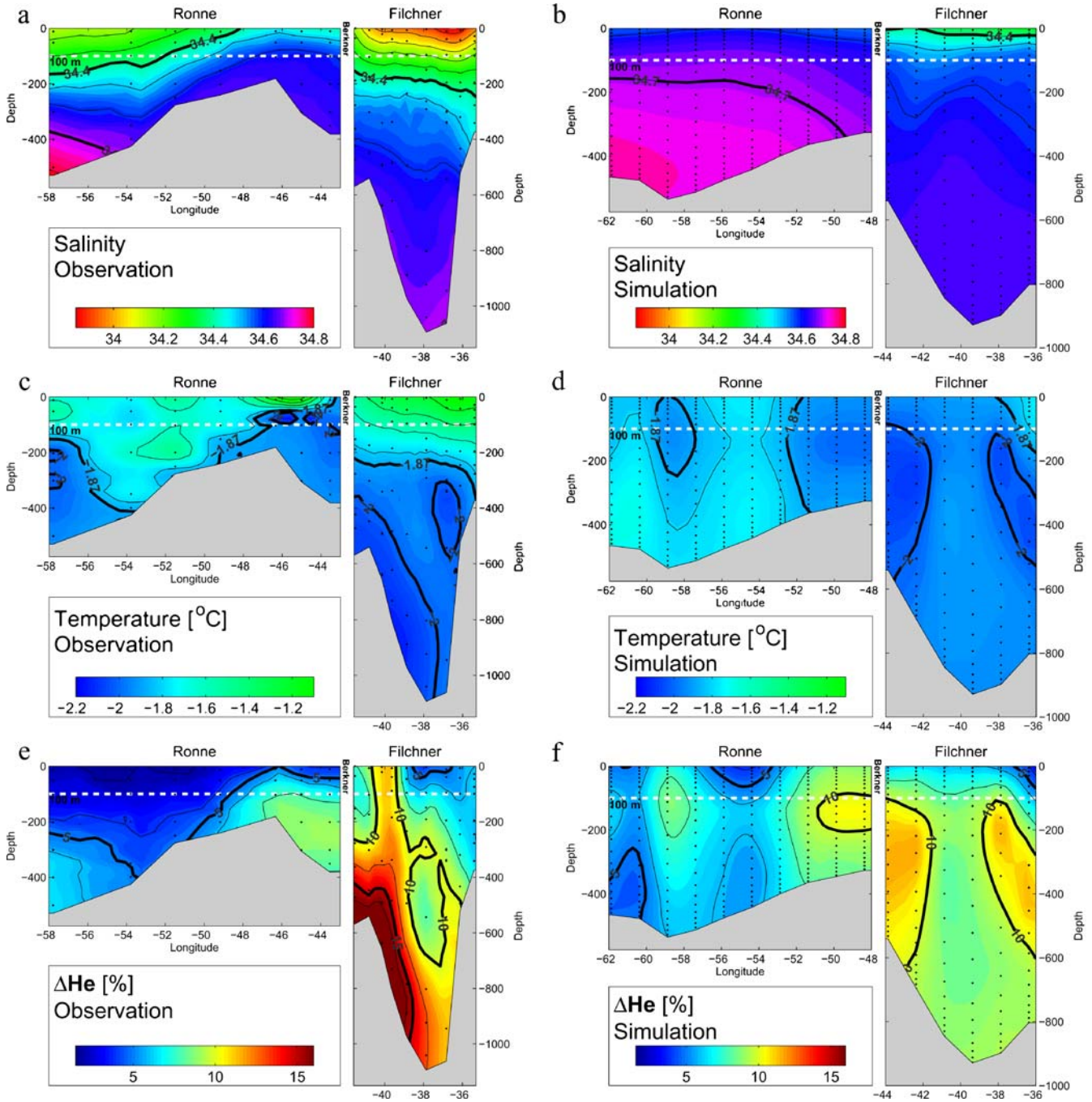

Fig. 4 Cross-sections of salinity (*upper*), potential temperature (*middle*), and helium supersaturation (*lower*) in front of Filchner–Ronne Ice Shelf (Fig. 3). The *left column* (**a**, **c**, **e**) shows the observations up to 58°W, while the *right column* (**b**, **d**, **f**) represents the simulated distribution along the entire ice edge on 1 January of year 60 (since the release of the tracer). *Black dots* mark sample location or model grid point in the water column. *Colorbars* are identical for observations and simulations. *Thick contour lines* are: S= 34.4, 34.7, Θ= –1.87°C, –2°C, and ΔHe= 5%, 10%, 15%. The *white dashed line* indicates the cut-off depth at 100 m, above which values are excluded from the analysis as explained in the text

southern continental shelf to the east and west, as described by Grosfeld et al. (2001) and Nicholls et al. (2003), respectively, can be summarized as follows: a general east to west advection of shelf waters along the ice shelf front in combination with a continuous salt gain due to sea ice formation causes high salinities near the Antarctic Peninsula (Fig. 4a,b). Here, the main flow underneath FRIS takes place, feeding most of the cavern's ISW plumes (Nicholls and Østerhus 2004).

The main ISW outflow occurs on the western slope of the Filchner Trough with observed helium supersaturations of up to ΔHe ≈ 20% (Fig. 4c–f). The less supersaturated

core on the eastern flank can be associated with the return flow as part of the cyclonic trough circulation (Nicholls and Østerhus 2004). The observed ISW cores—areas of maximum ΔHe and minimum Θ —are deeper, and modeled saturations are significantly lower, both for reasons discussed below.

On the continental shelf west of Berkner Island, a shallow ISW core was observed with supersaturations of $\Delta\mathrm{He} = 9.7\%$ and $\Delta\mathrm{Ne} = 7.1\%$, which are lower than the simulated values, $\Delta\mathrm{He} = 10.2\%$ and $\Delta\mathrm{Ne} = 7.7\%$. The model results indicate that this core is not influenced by the deeper core in the Filchner Trough but is fed by a direct outflow from the Ronne Ice Shelf cavern (compare Fig. 9). An additional but weaker ISW core was observed at the western Ronne Ice Shelf edge below 300 m. Although at the same longitude, the simulated core is shallower by about 100 m. Its higher supersaturation might be explained by the measurements not covering the entire Ronne Depression. The ISW cores are clearly visible in the sections of potential temperature but hardly traceable in the salinity distributions along the ice shelf edge (Fig. 4a–f). This is caused by the strong dependency of density on salinity for waters below the surface freezing point, forcing the ISW plume to stratify at the appropriate density/salinity horizon and, thus, losing any dominant freshwater signal in the water column.

The amount of noble gases released and the strength of the supersaturation signal in the outflows are both proportional to the melting at the ice shelf base. Although the model is forced with a recurring annual cycle, basal melting beneath FRIS varies between 119 km^3 /a (cubic meter per year) and 143 km^3 /a around a mean value of 130 km^3 /a (Fig. 5). This mean is larger than the maximum net melt rate beneath FRIS of 118 km^3 /a derived from

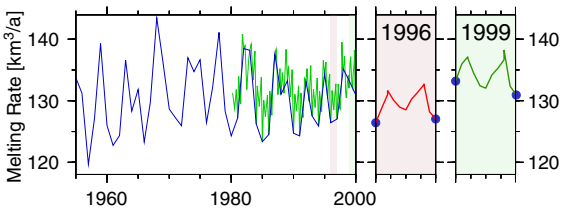

Fig. 6 Melt rate for Filchner–Ronne Ice Shelf for a 45-year period (*left*). The *blue line* connects values of 1 January of each year, the *green line* connects monthly means of the second half of this period. Two different arbitrary chosen annual melt rate cycles (*right*). The unit is km ^{3} /year with 100 km^3 /a ≈ 3 mSv

remote-sensing data (Joughin and Padman 2003) but smaller than the 157 km^3 /a estimated from δ^{18}O in the ISW plume off Filchner (Schlosser et al. 1990); both values are based on an ice density of 917 kg/m^3 . The interannual variability (despite a constant annual surface forcing) results from the exchange between outflowing and inflowing water masses in front of the ice shelf (Nicholls 1997) and the time a signal imprinted on the continental shelf needs to traverse the sub-ice cavern. The amplitude of the annual melt cycle is smaller than the total variability of melting (Fig. 5). Therefore, we assume that the 50-year mean represents the noble gas distribution in front of FRIS fairly well, taking into account that the seasonal change of the hydrographic properties below 100 m affects the noble gas saturation in the meltwater plume by less than 0.1%.

In the following, we compare measured with modeled salinity/temperature vs helium supersaturation in front of FRIS (Fig. 6). Due to the different oceanographic regimes on the southern Weddell Sea continental shelf, the results are separated for Filchner (east) and Ronne (west).

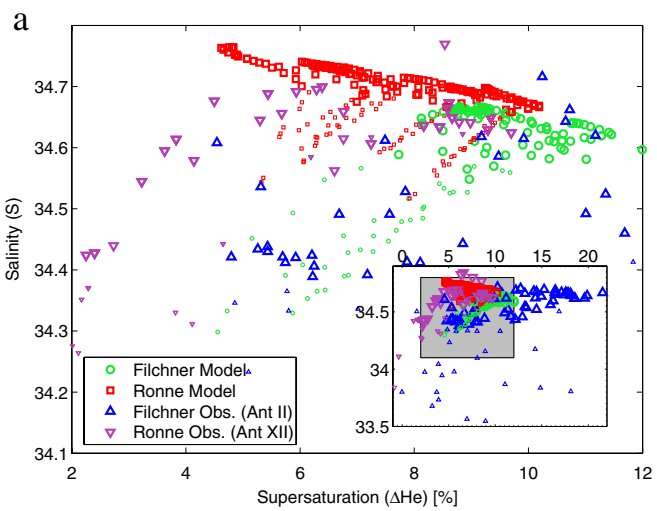

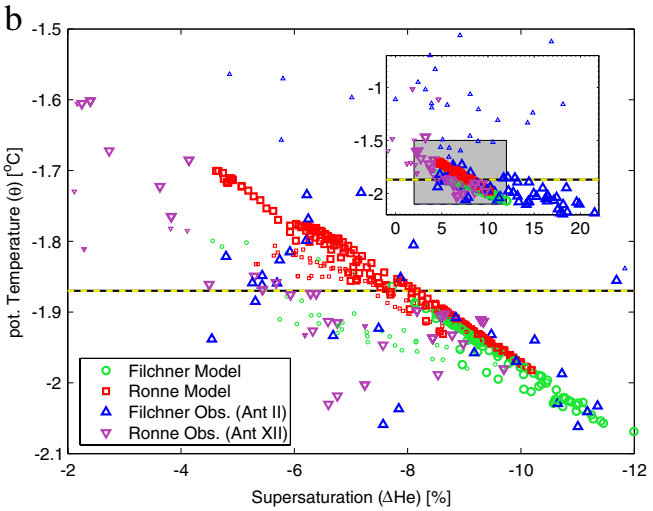

Fig. 5 Salinity vs helium supersaturation (*left*) and temperature vs helium supersaturation (*right*) diagrams for the whole water column on the southern Weddell Sea continental shelf separated into the Filchner (east) and Ronne (west) regimes. The *larger diagrams* cover the simulated values, while the *insets* show the entire range of the measurements, with the *gray square* representing the range of the larger diagrams. The measurements are represented by *triangles*, while *circles* and *squares* represent simulated values of model year 60 (since the release of the tracer). *Smaller symbols* represent values of the uppermost 100 m, which are excluded from our analysis. The *yellow line* in **b** marks the surface freezing temperature (T_f)

3.1 Salinity vs helium supersaturation

The salinity–helium supersaturation values are clustered according to their origin (Fig. 6a) with higher salinities (higher helium supersaturation) representing the continental shelf in front of Ronne (Filchner) Ice Shelf. Considering the whole water column, three end members can be identified in the salinity–helium supersaturation (S -ΔHe) space:

1. Low S and low ΔHe
2. High S and low ΔHe
3. Low S and high ΔHe

The first end member represents the summer surface water masses of the upper 100 m, which, freshened by sea ice melting, contribute to the stabilization of the water column. The observed salinity covers a wider range because of a high interannual variability of the sea ice cover not captured by the model due to its time invariant surface forcing. Because the light surface water does not seem to mix with the ISW outflow (Fig. 6a), it will not be considered in the later discussion. The second end member characterizes HSSW, which results from deep convection driven by salt accumulation during sea ice formation. This process shifts the salinity (of end member 1) to higher values but keeps the helium supersaturation low due to gas exchange across the ocean–atmosphere interface. The third end member is the result of the continuous modification of HSSW at the ice shelf base (Fig. 1). The entrainment of glacial meltwater decreases the salinity, while the complete solution of the gases released by melting increases the helium supersaturation.

The modeled values along the FRIS edge qualitatively agree with the observations with the upper 100 m of the water column, covering a wider range than further below. The salinity–helium supersaturation range, however, is smaller, and the helium maximum in front of Filchner Ice Shelf is half the observed value (see also Fig. 4e–f). This difference can be explained by the narrowness (15–50 km) of the ISW plume in the Filchner Trough (Schlosser et al. 1990), which cannot be captured in detail by a model resolution of ~ 24 km at the FRIS front. In contrast, the lower maximum supersaturation related to the broader ISW flow out of the Ronne cavern (west of Berkner Island) is better represented by the simulation.

3.2 Temperature vs helium supersaturation

In front of Filchner Ice Shelf (Fig. 6b), observed temperature vs helium relations below 100 m are grouped along a straight line with a minimum temperature of $-2.19°C$ and a maximum supersaturation of $\Delta\mathrm{He} = 21.5\%$ (Figs. 2 and 5 in Schlosser et al. 1990). Such straight line is common for temperature vs salinity distributions in front of ice shelves representing the melting of meteoric ice into seawater (Gade 1979). Deviations from this line mainly represent water of the upper 100 m, which includes a significant amount of warmer surface waters. Because the model resolution is coarse and it is driven with a smooth annual cycle, the observed relations scatter more around the regression line (Fig. 7). The observed correlations are almost 10–50% lower than for the simulation (Table 1). In front of the Ronne Ice Shelf, the supersaturations are smaller with a maximum of $\Delta\mathrm{He} = 9.70\%$ and temperatures are higher with a minimum of $-2.03°C$ close to Berkner Island (Figs. 4d and 6b).

3.3 Calculation of properties of the melt-free component

The Foldvik process considers newly formed bottom water as a mixture of helium and neon supersaturated ISW with nearly 100% ($\Delta\mathrm{He}, \Delta\mathrm{Ne} = 0$) saturated ambient water masses. To specify the ambient waters in the southern Weddell Sea, we determine the temperature and salinity of the glacial melt-free component by calculating the regression line based on observed and modeled data points of the temperature/salinity–helium supersaturation spaces below 100 m. The line's intercept with the ordinate ($\equiv$ 0% supersaturation) provides the temperature/salinity of the ambient water. For the analysis, we used the samples at the locations depicted in Fig. 3 and the temporal means of all open ocean grid points adjacent to the FRIS edge calculated from the data of 1 January of model years 30–80 (since the release of the tracer). The standard deviation for the temporal means is considered as uncertain. For the data set of each year (years 30–80 since release of the tracer), we calculated a regression line. The envelopes of these regression lines represent the model's uncertainty for the properties of the glacial melt-free component.

The simulated salinity/temperature vs helium supersaturation values are located within the cluster of measured values (Fig. 7a,b). The maximum standard deviation for supersaturation, considering all model grid points for the year 30–80 period, of 1.06% exists in front of Filchner Ice Shelf at a depth of 218 m. For temperature and salinity, maximum standard deviations of $0.05°C$ and 0.019 occur at depths of 183 and 163 m, respectively, in front of Ronne Ice Shelf. This spatial separation of the variability for different characteristics is evidence for the Ronne regime

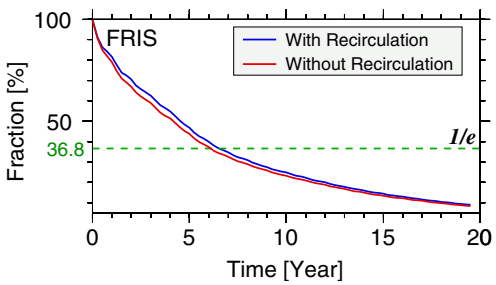

Fig. 7 Temporal evolution of an artificial tracer concentration within FRIS. A water parcel is considered "recirculated" if it retains its initial signature after leaving and reentering the cavern. The residence time (e-folding time) is 6.5 or 6 years by considering or neglecting recirculation

Table 1 Characteristics of the glacial-melt free component as intercepts at zero supersaturation and slopes of the linear regression through the pairs of temperature/salinity and helium supersaturation as depicted in Fig. 8a,b for all data ("All") and separated for the "Filchner" and "Ronne" regimes

Area	Intercept		Δ	Slope/100		Correlation coefficient (%)	
	Observation	Simulation		Observation	Simulation	Observation	Simulation
Salinity–supersaturation relation							
Filchner	34.38±0.05	34.76±0.00	−0.38	1.5±0.45	−1.24±0.02	70	−43
Ronne	34.53±0.04	34.83±0.00	−0.3	1.4±0.5	−1.542±0.004	80	−90
All	34.57±0.03	34.86±0.03	−0.29	0.51±0.32	−2.137±0.005	23	−83
Temperature–supersaturation relation							
Filchner	−1.75±0.06	−1.486±0.001	−0.26	−1.90±0.43	−4.954±0.007	−76	−97
Ronne	−1.57±0.05	−1.475±0.001	−0.1	−4.3±0.6	−4.962±0.003	−46	−99
All	−1.70±0.03	−1.465±0.000	−0.24	−2.4±0.3	−5.129±0.003	−76	−99

The uncertainties represent the 95% confidence interval, while Δ is the intercept difference with Δ = observation − simulation

being dominated by shelf waters, while Filchner is mainly influenced by the outflow of glacial meltwater. In addition, ocean/ice shelf interaction in the cavern seems to dampen the variability of the inflow characteristics (temperature and salinity) and to convert the fluctuations to a variability of noble gas saturation in the outflowing meltwater plume.

Along the FRIS front, the model tends to overestimate temperature and salinity of the glacial melt-free component penetrating onto or already on the continental shelf as shown in Table 1. This is mainly caused by the model resolution insufficient to capture the narrow cold ISW outflows and the topography at the continental shelf break, which blocks warm open-ocean waters from access to the continental shelf, and by the forcing with the output of a stand-alone sea ice model. The latter simulates a permanent sea ice cover in front of FRIS, reducing the salt released during sea ice formation with consequences for deep convection and the cooling of the shelf water column.

On the other hand, Southern Ocean observations are affected by long-term variability. The measurements in front of Filchner Ice Shelf (*ANT III*, 1985) were conducted during a phase of the Antarctic Circumpolar Wave (ACW), with positive temperature and negative sea ice coverage anomalies in the southwestern Weddell Sea related to weaker southerly winds (White and Peterson 1996). In contrast, data off the Ronne Ice Shelf (*ANT XII/3*, 1995) were collected during negative temperature and positive sea ice coverage anomalies related to stronger southerly winds, which enhanced the salt input and deep convection. The latter increases at depth the amount of water that was recently in contact with the atmosphere at temperatures equal to the surface freezing point (T_f), but decreases the relative amount of ISW with temperatures below surface freezing. Therefore, for a continental shelf influenced by ISW outflow, enhanced convection may lead to a warming of the lower water column. Whether such mechanism caused the smaller temperature difference between model results and observations in front of the Ronne Ice Shelf remains speculative.

The correlations for salinity and helium supersaturation show a nonuniform picture, being positive for the observations and negative for the simulation. In addition,

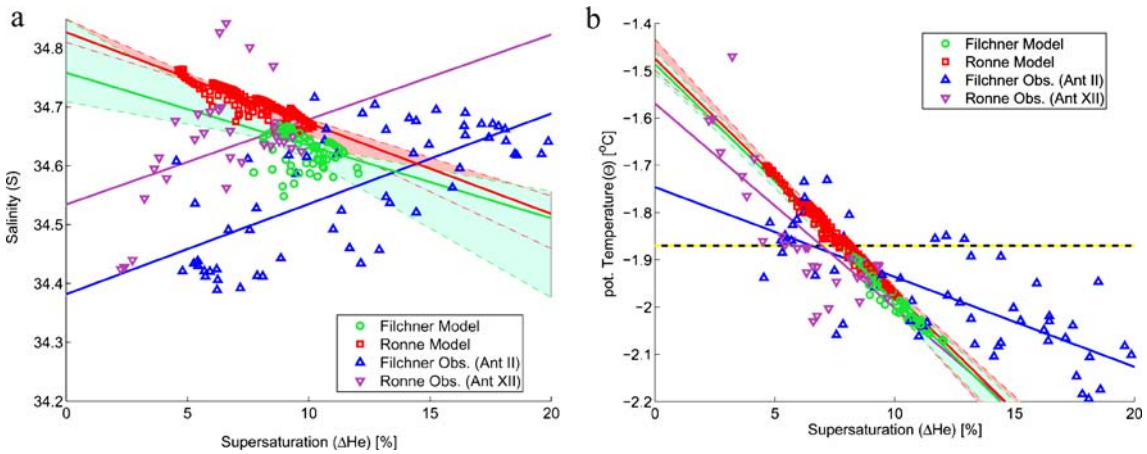

Fig. 8 Salinity vs helium supersaturation (*left*) and temperature vs helium supersaturation (*right*) diagrams for the water column below 100 m on the southern Weddell Sea continental shelf separated into the Filchner (east) and Ronne (west) regimes. The *x*-coordinate was extended to zero supersaturation to determine the salinity and potential temperature of the melt-free component using a linear regression. Measurements are represented by *triangles*, while *circles* and *squares* represent means of model years 30–80 since tracer release. The *colors* of the linear regression lines correspond to the colored data points. The *yellow line* in the right figure marks the surface freezing temperature T_f

both correlations for Ronne are higher than those for Filchner (Table 1). The latter is additional evidence for the regional separation between main inflow and main outflow for the FRIS cavern. The correlation between temperature/salinity of the inflow (Ronne) and helium supersaturation of the outflow (Filchner) is also low (not shown). However, since results before model equilibrium indicated the sub-ice transit of a long-term trend, we suggest a "low-pass" filtering within the cavern, supported by a multiyear residence time (Bayer and Schlosser 1991; Mensch et al. 1996), in combination with mixing between water masses of different age (Fig. 8).

The addition of melt water, characterized by high supersaturations, reduces the salinity of the outflow. The model reproduces this combination even when the correlation is weak in front of Filchner (Table 1). The observations show instead that higher supersaturations are correlated with higher salinities. However, if we consider all data in front of FRIS, the correlation is very weak (Table 1). In contrast, the combination of cooling due to melting and higher supersaturations in the ISW plume is clearly detectable by observed and modeled Θ and ΔHe everywhere along the FRIS front (Fig. 4). One possibility for this discrepancy could be that the observations did not cover the saltiest shelf waters predominantly located in the westernmost corner of the southern continental shelf close to the Antarctic Peninsula. However, further study needs to be done to understand the observed positive correlation between salinity and helium supersaturation.

4 Spreading of ISW

A meltwater plume carries a higher helium than neon supersaturation signal due to a lower solubility for helium. Far from the source, the glacial-melt helium signal is, however, difficult to separate from a helium signal originating from other sources (Roether et al. 1998, 2001), like crust (crustal) and mantle (primordial) helium. Therefore, neon is a more suitable tracer to pursue glacial melt in the ocean because the atmosphere/ocean exchange (Ozima and Podosek 1983) and ice shelf melting (Schlosser 1986) are the only sources. In the following, we analyze the spreading of water masses containing ISW in the Southern Ocean by simulating circumpolar helium and neon distributions. In addition, we discuss the importance of neon as an oceanic tracer.

The ISW spreading path, assuming an accuracy of the measurements of 0.2%, is shown in Fig. 9. The largest bottom patch with a significant supersaturation signal occurs in the southwestern Weddell Sea. Sources are the Brunt–Riiser–Larsen– (BRILIS), Filchner–Ronne, and Larsen Ice

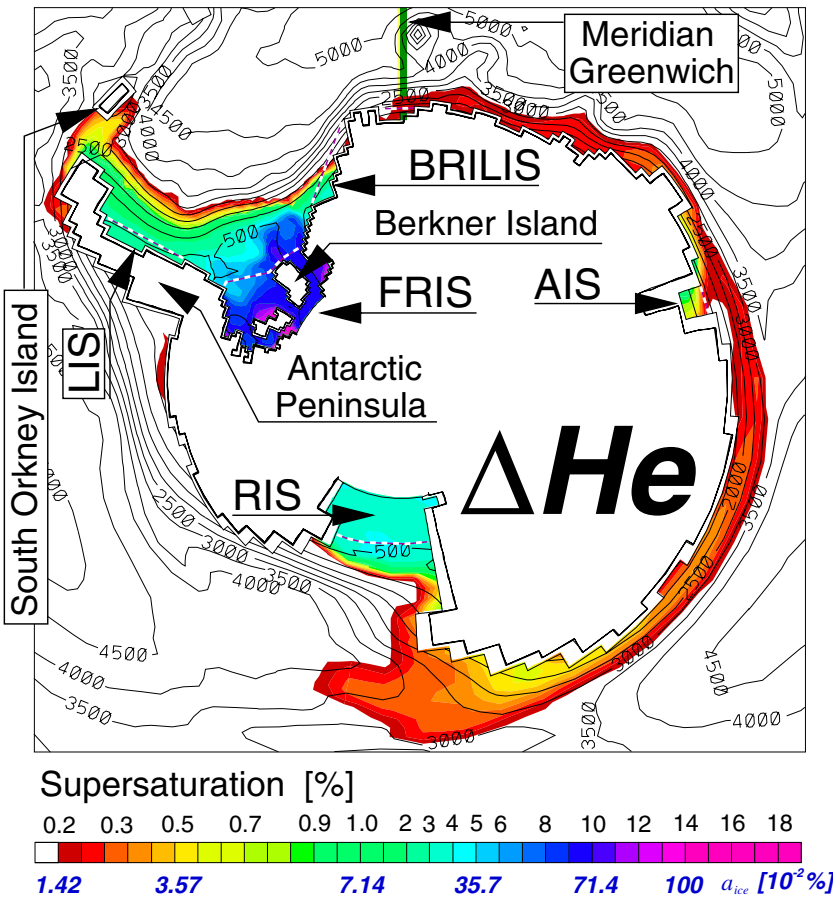

Fig. 9 Modeled (year 50 since tracer release) supersaturations of helium in the bottom layer of the Southern Ocean together with the freshwater fraction (*lower legend*) from ice shelf melting deduced from the helium supersaturation according to Eq. 4. The figures include the ice shelf fronts as represented in the model (*white/magenta lines*), bottom topography (*black lines*) with contour intervals of 500 m, and ice shelf names. *FRIS* Filchner–Ronne Ice Shelf, *BRILIS* Brunt–Riiser–Larsen Ice Shelf, *AIS* Amery Ice Shelf, *LIS* Larsen Ice Shelf, *RIS* Ross Ice Shelf

Shelves (from east to west). The BRILIS signal spreads westward with the coastal current toward the sill of the Filchner Trough, where it encounters the stronger supersaturation signal from FRIS. In agreement with the observations in front of the Ronne Ice Shelf ("Model validation" section) and from the southern Weddell Sea continental shelf (Gammelsrød et al. 1994; Foldvik et al. 1985a,b; Mensch et al. 1996; Nicholls and Makinson 1998; Nøst and Østerhus 1998), an additional supersaturation signal appears west of Berkner Island (Fig. 9). Although in Ronne Basin close to the Antarctic Peninsula higher helium and neon supersaturations also exist, the signals are smaller than in the Filchner Trough (helium 6–7% vs 9–10%, neon 4–5% vs 7–8%). On the way to the northwestern Weddell Sea, as part of the cyclonic gyre circulation, Larsen Ice Shelf adds a tracer signal, which is, however, not strong enough to overwhelm the supersaturation signal from FRIS. Helium- and neon-rich waters pass the northern tip of the peninsula to flow either westward in the southern Drake Passage as part of a slope current (Nowlin and Zenk 1988) or eastward within the northern limb of the Weddell Gyre (Fig. 9). In the Ross Sea, ISW-rich water follows the circulation of the Ross Gyre (e.g., Assmann and Timmermann 2005) as far as Cap Adare (western tip), where the signal splits into two branches (Fig. 9). One advects with the Ross Gyre to the east, slowly eroding due to mixing with lower saturated waters. The other branch flows westward with the coastal current being detectable up to Prydz Bay in front of Amery Ice Shelf. The Amery signal is clearly distinguishable from the RIS signal, as it dominates the supersaturation in Prydz Bay. Since it also mixes into the Antarctic Coastal Current, it can be traced as far as the Greenwich Meridian (eastern Weddell Sea) (Fig. 9).

The isotope laboratory at the University of Bremen (Institute for Environmental Physics) measures neon data with a precision (internal consistency) of 0.1–0.3% (Well 1995; Well and Roether 2003). For a currently supposed detectable supersaturation of 0.5–1%, ISW can be only found in the bottom layer on the continental shelf in front and next to the major caverns (Fig. 9); i.e, northwest of the Amery Ice Shelf, in a narrow band along the Ross Ice Shelf front, and in the Weddell Sea, where the large supersaturated patch completely erodes as it reaches the northern tip of the Antarctic Peninsula. An enhanced detectability would improve the representation of ISW flows in the Southern Ocean especially for those originating from the Ross and Amery ice shelves.

4.1 Melt water fraction along the ISW spreading path

The fraction of meltwater a_{ice} within the water column along the ISW spreading path can be calculated based on helium and/or neon concentrations, assuming the water to be formed by a two-component mixture—one part supersaturated ISW and the other part ambient water saturated by 100%:

$$c_{\mathrm{obs}} = a_{\mathrm{ice}}\hat{S}c_0 + (1 - a_{\mathrm{ice}})c_0$$

$$a_{\mathrm{ice}} = \frac{1}{15}\left(\frac{c_{\mathrm{He}}}{c_0} - 1\right) \tag{4}$$

$$a_{\mathrm{ice}} = \frac{1}{10.6}\left(\frac{c_{\mathrm{Ne}}}{c_0} - 1\right). \tag{5}$$

Here, c_0 is the saturation concentration, and c_{He} and c_{Ne} are the (observed) concentrations of helium and neon. The constants on the right-hand side result from the saturation ($\hat{S}$) of helium and neon of 1,500 and 1160% (100% saturation and supersaturation of pure glacial meltwater of 1,400 and 1,060%; Schlosser 1986) due to ice shelf melting. We expect that the saturation concentrations of the ambient water masses are identical, which is valid for water masses at nearly the same temperature. For the assumption of a two-component mixture, a supersaturation in helium (neon) of 10% is equivalent to a meltwater fraction of 0.714% (0.943%) (see color bar in Fig. 9). High meltwater fractions of $a_{\mathrm{ice}} \approx 0.7\%$ were observed in the water column directly in front of Filchner Ice Shelf (Schlosser et al. 1990). The fraction a_{ice}, however, reduces to 0.01% on its way from the source area to the South Orkney Islands. Enhanced turbulent mixing along the rough topography of the South Scotia Ridge continues to erode the meltwater signal such that an improved accuracy of the measurements might only have a limited effect on a better identification of ISW spreading within the northern limb of the Weddell Gyre.

5 Conclusions

For the first time, a regional ocean circulation model, which includes the interaction between ice shelves and ocean, is used to determine the release of noble gases, helium, and neon due to ice shelf basal melting. Noble gases are ideal for tracing the meltwater embedded in Ice Shelf Water, which contributes to the formation of bottom water in the Southern Ocean and, thus, to the ventilation of the global abyss. Although helium has a stronger supersaturation signal, we recommend neon to be used for this procedure due to its simple input function.

The comparison between modeled and observed temperature/salinity vs helium supersaturation relations in front of FRIS shows that the model reproduces the

characteristic features on the southwestern Weddell Sea continental shelf, i.e., increasing salinity from east to west, lowest temperatures combined with highest supersaturations in the Filchner Trough, and a cavern circulation with main inflow at the Ronne and main outflow at the Filchner ice fronts. The discrepancy between the observed and modeled characteristics of the glacial melt free components might be caused in part by the fact that the observations were conducted at different phases of the ACW. However, model deficiencies with regard to resolution of bottom topography on the continental shelf and the forcing with the output of a stand-alone sea ice model might have even a bigger impact on the model's deviation from the observations. Although forced with a recurring annual cycle, the water mass characteristics on the continental shelf, as well as the net basal mass loss, fluctuate during the 60-year integration, caused by a feedback mechanism on time scales of several years between the ice shelf cavern and the continental shelf. The freshwater flux originating from FRIS has an impact on shelf water salinity and sea ice thickness (Hellmer 2004) and, therefore, on the composition of the water masses feeding the meltwater plume from beneath the ice shelf.

Our model results support the general perception that ocean–ice shelf interaction has a significant influence on the characteristics of deep and bottom water. However, to provide a more comprehensive picture of the deep and bottom water formation in Antarctic marginal seas processes that occur in the open ocean also have to be considered. We therefore prepare an analysis of the results of a transient chlorofluorocarbon simulation (Rodehacke et al., 2006, in preparation).

In general, noble gas measurements are an excellent tool to study the cavern–continental shelf interaction because they are less susceptible to environmental changes, which occur on interannual time scales. The current accuracy of measurements allows for the detection of ISW only close to the fronts of the major Antarctic ice shelves. Our model results indicate that with enhanced detectability of 0.2%, the spreading paths of water masses containing traces of glacial melt/ISW could be easier to determine beyond the source areas. The meltwater signal from Filchner–Ronne Ice Shelf could be traced within the northern limb of the Weddell Gyre with access to the Scotia Sea. Traces of ISW originating from the Ross Ice Shelf would be detectable as far as the Prydz Bay. Here, the outflow from the Amery Ice Shelf dominates the meltwater signal, which advects with the coastal current toward the Weddell Sea having a still clear signal at the Greenwich Meridian. This occurrence provides additional evidence for a flow of freshly ventilated water masses into the Weddell Sea at 3,000–4,000 m depth (characterized by high CFC concentrations; Klatt et al. 2002), influenced by the processes in front of Amery Ice Shelf, as already suggested by the model results of Schodlok et al. (2001).

Our model approach neglects the influence of sea ice formation on the saturation of noble gases in the mixed layer. It is still debatable whether a reduction of the saturation due to sea ice formation has an impact on the neon concentration in freshly ventilated water masses of the deep ocean. Hood (1997) and Hood et al. (1998) suggest that sea ice formation erodes the neon supersaturation originating from ocean/ice shelf interaction, though Well and Roether (2003) argue that such strong neon reduction is not consistent with tracer observations in the Southern Ocean. Therefore, we further have to speculate about the processes, which cause the observed slight supersaturation of neon in the abyssal ocean. One process might be the partial pressure change during the solution of noble gas in the mixed layer and its subduction (Hamme and Emerson 2002). Our model results suggest that the influence of the ocean–ice shelf interaction on the neon supersaturation in newly formed deep and bottom water cannot be further neglected. However, models with higher resolution and improved physics regarding the parameterization of the ocean–sea ice interaction and vertical mixing, and an adequate representation of descending plumes at the continental slope are necessary to satisfactorily address the importance of the glacial meltwater for the water mass characteristics of the Southern Ocean.

Acknowledgements We thank W. Roether and his former group at University Bremen for providing the noble gas data and supporting the completion of the manuscript in various ways. Thanks also to three reviewers, whose invaluable criticism helped to clarify and improve the manuscript. We thank R. Timmermann and C. Lichey for providing model forcing fields. C. Rodehacke thanks B. Klein and the team of the Institute for (Tracer) Oceanography at University of Bremen for their contribution to the data processing. This project was funded by the Deutsche Forschungsgemeinschaft (DFG) Nr. Ro 318/43 and the Alfred-Wegener-Institute contribution n15744.

References

Asher W, Wanninkhof R (1998) Transient tracers and air–sea gas transfer. J Geophys Res 103(C8):15939–15958

Assmann K, Timmermann R (2005) Variability of dense water formation in the Ross Sea. Ocean Dyn 55(2):68–87

Baines P, Condie S (1998) Observations and modelling of Antarctic downslope flows: a review. In: Jacobs S, Weiss R (eds) Ocean, ice and atmosphere: interaction at the antarctic continental margin. Antarctic Research Series, vol. 75. American Geophysical Union, Washington, pp 29–49

Bayer R, Schlosser P (1991) Tritium profiles in the Weddell Sea. Mar Chem 35:123–136

Beckmann A, Hellmer H, Timmermann R (1999) A numerical model of the Weddell Sea: large scale circulation and water mass distribution. J Geophys Res 104(C10):23375–23391

Carmack E (1974) A quantitative characterization of water masses in the Weddell Sea during summer. Deep-Sea Res 21:431–443

England MH, Garcon V, Minster J-F (1994) Chlorofluorocarbon uptake in a world ocean model 1. Sensitivity to the surface gas forcing. J Geophys Res 99(C12):25215–25233

Foldvik A, Gammelsrød T, Tørrensen T (1985a) Hydrographic observations from the Weddell Sea during the Norwegian Antarctic research expedition 1976/77. Polar Res 3:177–193

Foldvik A, Gammelsrød T, Tørresen T (1985b) Circulation and water masses on the southern Weddell Sea shelf. In: Jacobs SS (ed) Oceanology of the Antarctic continental shelf. Antarctic Research Series, vol. 43. American Geophysical Union, Washington, pp 5–20

Foster T, Carmack E (1976) Frontal zone mixing and Antarctic bottom water formation in the southern Weddell Sea. Deep-Sea Res 23:301–317

Gade H (1979) Melting of ice in seawater: a primitive model with application to the Antarctic ice shelf and icebergs. J Phys Oceanogr 9:189–198

Gammelsrød T, Foldvik A, Nøst O, Skagseth Ø, Anderson L, Fogelqvist E, Olsson K, Tanhua T, Jones E, Østerhus S (1994) Distribution of water masses on the continental shelf in the southern Weddell Sea. In: The polar oceans and their role in shaping the global environment. Geophysical Monograph, vol. 84. American Geophysical Union, Washington, pp 159–176

Gerdes R, Determann J, Grosfeld K (1999) Ocean circulation beneath Filchner–Ronne Ice Shelf from three-dimensional model results. J Geophys Res 104(C7):15827–15842

Grosfeld K, Schröder M, Fahrbach E, Gerdes R, Mackensen A (2001) How iceberg calving and grouding change the circulation and hydrography in the Filchner Ice Shelf–Ocean System. J Geophys Res 106(C5):9039–9055

Haidvogel DB, Wilkin JL, Young R (1991) A semi-spectral primitive equation ocean circulation model using vertical sigma and orthogonal curvilinear horizontal coordinates. J Comput Phys 94(1):151–185

Hamme R, Emerson S (2002) Mechanisms controlling the global oceanic distribution of the inert gases: argon, nitrogen and neon. Geophys Res Lett 29(23):1–4

Hamme R, Emerson S (2004) The solubility of neon, nitrogen and argon in distilled water and seawater. Deep-Sea Res 51 (11):1517–1528

Hellmer H (2004) Impact of Antarctic ice shelf melting on sea ice and deep ocean properties. Geophys Res Lett 31(10):28–29

Hellmer H, Olbers D (1989) A two-dimensional model for the thermohaline circulation under an ice shelf. Antarct Sci 1: 325–336

Hohmann R, Schlosser P, Jacobs S, Ludin A, Weppernig R (2002) Excess helium and neon in the Southeast Pacific: tracers for glacial meltwater. J Geophys Res 107(C11):3198

Hood E (1997) Characterization of the air–sea gas exchange processes and dissolved gas/ice interaction using noble gases. Disseration, Massachusetts Institute of Technology/Woods Hole Oceanographic Institution, Cambridge, MA, USA

Hood E, Howes B, Jenkins W (1998) Dissolved gas dynamics in perennially ice-covered Lake Fryxell, Antarctica. Limnol Oceanogr 43(2):265–272

Jähne B, Heinz G, Dietrich W (1987) Measurement of the diffusion coefficients of sparingly soluble gases in water. J Geophys Res 92(C10):10767–10776

Joughin I, Padman L (2003) Melting and freezing beneath Filchner–Ronne Ice shelf, Antarctica. Geophys Res Lett 30(9):1477

Klatt O, Roether W, Hoppema M, Bulsiewicz K, Fleischmann U, Rodehacke C, Fahrbach E, Weiss R, Bullister J (2002) Repeated CFC sections at the Greenwich Meridian in the Weddell Sea. J Geophys Res 107(C4):43

Lewis E, Perkin R (1985) The winter oceanography of McMurdo Sound, Antartica. In: Jacobs S (ed) Oceanology of the Antarctic Continental Shelf. Antarctic Research Series, vol. 43. American Geophysical Union, Washington, pp 145–166

Mensch M, Bayer R, Bullister J, Schlosser P, Weiss R (1996) The distribution of tritium and CFCs in the Weddell Sea during the Mid 1980s. Prog Oceanogr 38:377–415

Nicholls K (1997) Predicted reduction in basal melt rates of an Antarctic ice shelf in a warmer climate. Nature 388:460–462

Nicholls K, Makinson K (1998) Ocean circulation beneath the Western Ronne Ice Shelf, as derived from in situ measurements of water currents and properties. In: Jacobs S, Weiss R (eds) Ocean, ice and atmosphere: interaction at the antarctic continental margin. Antarctic Research Series, vol. 75. American Geophysical Union, Washington, pp 301–318

Nøst O, Østerhus S (1998) Impact of grounded icebergs on the hydrographic conditions near the Filchner Ice Shelf. In: Ocean, ice and atmosphere: interaction at the Antarctic continental margin. Antarctic Research Series, vol. 75. American Geophysical Union, Washington, pp 267–284

Nicholls K, Østerhus S (2004) Interannual variability and ventilation time scales in the ocean cavity beneath Filchner–Ronne Ice Shelf, Antarctica. J Geophys Res 109(C04014)

Nicholls K, Padman L, Schrøder M, Woodgate R, Jenkins A, Østerhus S (2003) Water mass modification over the continental shelf north of Ronne Ice Shelf, Antarctica. J Geophys Res 108(C8):3260

Nowlin W Jr, Zenk W (1988) Westward bottom currents along the margin of the South Shetland Island Arc. Deep-Sea Res 35 (2):269–301

Olbers D, Gouretski V, Seiß G, Schröter J (1992) Hydrographic atlas of the southern ocean. Technical report, Alfred-Wegener-Institut for Polar and Marine Science, Bremerhaven, Germany

Ozima M, Podosek F (1983) Noble gas geochemistry. Cambridge University Press, USA

Roether W, Well R, Putzka A, Rueth C (1998) Component separation of oceanic helium. J Geophys Res 103 (C12):27931–27946

Roether W, Well R, Putzka A, Rueth C (2001) Corretion to "component separation of oceanic helium". J Geophys Res 106 (C3):4679

Schlosser P (1986) Helium: a new tracer in Antarctic oceanography. Nature 321:233–235

Schlosser P, Bayer R, Foldvik A, Gammelsrød T, Rohardt G, Münnich K (1990) Oxygen 18 and helium as tracers of ice shelf water and water/ice interaction in the Weddell Sea. J Geophys Res 95(C3):3253–3263

Schodlok M, Rodehacke C, Hellmer H, Beckmann A (2001) On the origin of the deep CFC maximum in the eastern Weddell Sea—numerical model results. Geophys Res Lett 28(14):2859–2862

Timmermann R, Beckmann A, Hellmer H (2002a) Simulations of ice–ocean dynamics in the Weddell Sea 1. Model configuration and validation. J Geophys Res 107(C3):101–109

Timmermann R, Hellmer H, Beckmann A (2002b) Simulations of ice–ocean dynamics in the Weddell Sea 2. Interannual variability 1985–1993. J Geophys Res 107(C3):111–116

Top Z, Eismont W, Clarke W (1987) Helium isotope effect and solubility of helium and neon in distilled water and seawater. Deep-Sea Res 34(7):1139–1148

Wanninkhof R (1992) Relationship between wind speed and gas exchange over the ocean. J Geophys Res 97(C5):7373–7382

Weiss R (1971) Solubility of helium and neon in water and seawater. J Chem Eng Data 16:235–241

Well R (1995) Analyse der Meßgüte eines massenspektrometrischen Meßsystems zur Heliumisotopen- und Neon-Bestimmung an Meerwasserproben. Disseration, Universität Bremen

Well R, Roether W (2003) Neon distribution in South Atlantic and South Pacific waters. Deep-Sea Res 50(6):721-735

White W, Peterson R (1996) An Antarctic circumpolar wave in surface pressure, wind, temperature and sea ice extent. Nature 380:699–702